Mitotic antipairing of homologous and sex chromosomes via spatial restriction of two haploid sets

Lisa L. Hua[a] and Takashi Mikawa[a,b,1]

[a]Cardiovascular Research Institute, University of California, San Francisco, CA 94158; and [b]Department of Anatomy, University of California, San Francisco, CA 94158

Edited by Jonathan Seidman, Harvard Medical School, Boston, MA, and approved November 14, 2018 (received for review June 5, 2018)

Pairing homologous chromosomes is required for recombination. However, in nonmeiotic stages it can lead to detrimental consequences, such as allelic misregulation and genome instability, and is rare in human somatic cells. How mitotic recombination is prevented—and how genetic stability is maintained across daughter cells—is a fundamental, unanswered question. Here, we report that both human and mouse cells impede homologous chromosome pairing by keeping two haploid chromosome sets apart throughout mitosis. Four-dimensional analysis of chromosomes during cell division revealed that a haploid chromosome set resides on either side of a meridional plane, crossing two centrosomes. Simultaneous tracking of chromosome oscillation and the spindle axis, using fluorescent CENP-A and centrin1, respectively, demonstrates collective genome behavior/segregation of two haploid sets throughout mitosis. Using 3D chromosome imaging of a translocation mouse with a supernumerary chromosome, we found that this maternally derived chromosome is positioned by parental origin. These data, taken together, support the identity of haploid sets by parental origin. This haploid set-based antipairing motif is shared by multiple cell types, doubles in tetraploid cells, and is lost in a carcinoma cell line. The data support a mechanism of nuclear polarity that sequesters two haploid sets along a subcellular axis. This topological segregation of haploid sets revisits an old model/paradigm and provides implications for maintaining mitotic fidelity.

homologous chromosomes | antipairing | mitosis | nuclear organization | haploid set segregation

Mitotic DNA recombination can be dangerous because of the high number of repeat sequences in the human genome that results in structural rearrangements and genome instability (1–3). Notably, recombination events can lead to loss of heterozygosity at specific gene loci and have been implicated in cancer initiation and progression (4, 5). To avoid this danger, recombination between nonallelic positions must be suppressed. One possible way of managing recombination may be limiting the potential pairing sites for recombination. Although homologous pairing in meiosis has been described in detail (6, 7), we know much less about the absence of pairing in mitosis.

It has been controversial whether homologous chromosomes are positioned antiparallel (8, 9) or distributed at random (10, 11) in human prometaphase cells. In this study, we revisit this unsolved but tantalizing question with many downstream implications. Methodologies that have been previously employed to analyze chromosome organization during mitosis include differential nucleotide detection by autoradiography (12), insertion of fluorescent repressive-operator arrays (13–15), photobleaching/photoactivation of fluorescently labeled histones (16–18), centromere marker-based tracing (19–21), and contrast-generating optical microscopy (22). Although these approaches provide a general observation of global chromosome organization, they lack detection for individual homologous chromosome pairs. To date, chromosome painting (23–25), the application of DNA probes specific to nonrepetitive sequences, has been a common and versatile technique to achieve simultaneous identification and visualization of homologous pairs. Employing this method, we systematically analyzed the spatial organization of all autosomal and sex chromosome pairs throughout mitosis.

Here, we report that homologous chromosomes are spatially segregated albeit without a defined position. We show that the spatial segregation is achieved by sequestering two haploid sets along specific cellular axes. Our data reconcile the current two contradictory models for the spatial organization of homologous pairs and propose a mechanism of antipairing between homologs during mitosis.

Results

Homologous Chromosomes Are Spatially Segregated Throughout Mitosis. For our initial survey of chromosome organization at prometaphase, the same stage analyzed in previous publications (8–11), chromosome paint probes were applied to human primary cells growing in a 2D cell-culture environment (Fig. 1 and *SI Appendix*, Fig. S1). We painted and mapped homologous pairs of various sizes (chromosomes 3, 4, 9, 11, and 18) in a simple epithelial cell type: human umbilical vein endothelial cells (HUVECs) (Fig. 1*A* and *SI Appendix*, Fig. S1 *B–G*). Two-dimensional culture of HUVECs displays clear apical/basal polarity (26). The spatial relationship between a homologous pair was determined by interhomolog angular measurement. If each homologous pair is positioned antiparallel to each other, an optimum/maximal angle of 180° will be obtained (8, 9). Our 3D reconstruction analysis of chromosome paint data revealed that

Significance

Mitotic recombination must be prevented to maintain genetic stability across daughter cells, but the underlying mechanism remains elusive. We report that mammalian cells impede homologous chromosome pairing during mitosis by keeping the two haploid chromosome sets apart, positioning them to either side of a meridional plane defined by the centrosomes. Chromosome oscillation analysis revealed collective genome behavior of noninteracting chromosome sets. Male translocation mice with a maternal-derived supernumerary chromosome display the tracer chromosome exclusively to the haploid set containing the X chromosome. This haploid set-based antipairing motif is shared by multiple cell types, is doubled in tetraploid cells, and is lost in carcinoma cells. The data provide a model of nuclear polarity through the antipairing of homologous chromosomes during mitosis.

Author contributions: L.L.H. and T.M. designed research; L.L.H. performed research; L.L.H. and T.M. analyzed data; and L.L.H. and T.M. wrote the paper.

The authors declare no conflict of interest.

This article is a PNAS Direct Submission.

[1]To whom correspondence should be addressed. Email: takashi.mikawa@ucsf.edu.

This article contains supporting information online at www.pnas.org/lookup/suppl/doi:10.1073/pnas.1809583115/-/DCSupplemental.

Published online December 10, 2018.

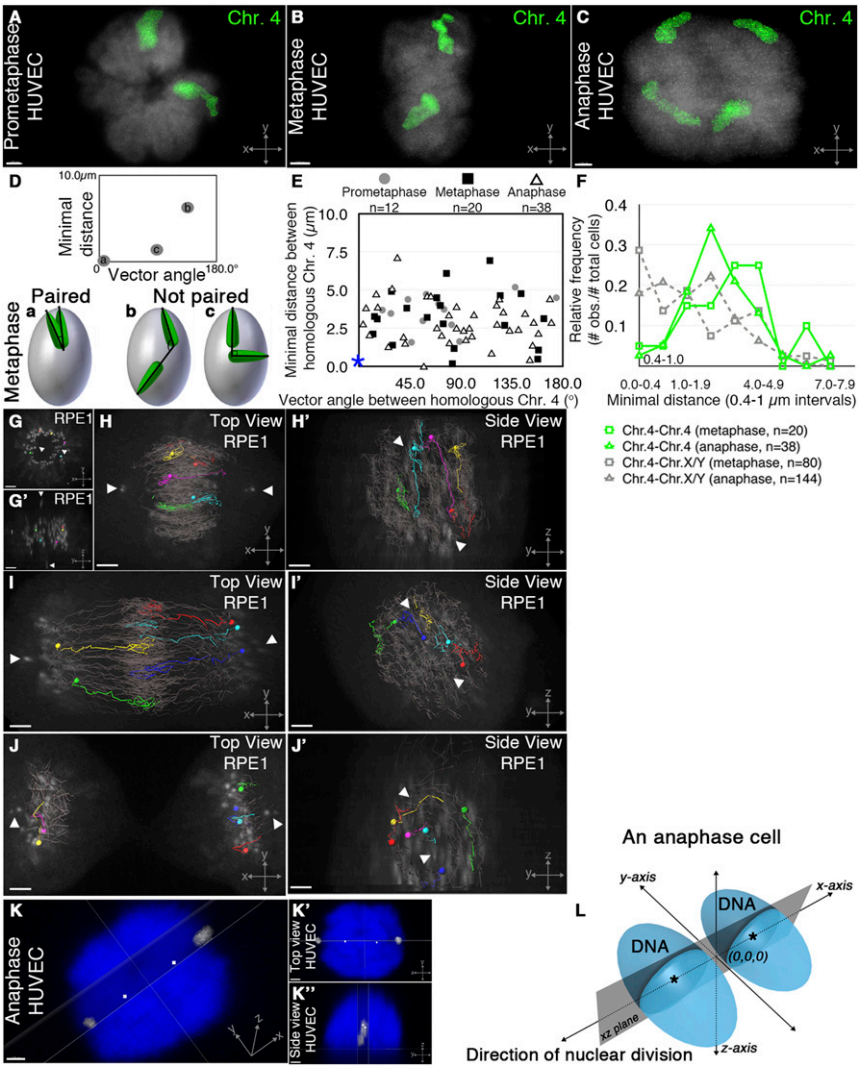

Fig. 1. Homologous chromosomes are spatially segregated throughout mitosis. (*A*–*C*) Top view of a HUVEC stained with TO-PRO3 (gray) and painted for chromosome 4 (green) from confocal optical sections at (*A*) prometaphase, (*B*) metaphase, and (*C*) anaphase. (*D*) Graphical examples of homologous chromosome pairing and no pairing with respect to distance and angular orientation measurements. (*a*–*c*) Schematic for determination of measurements. (*E*) Distance and angular orientation for each pair of homologous chromosome 4 data points at prometaphase ($n = 12$), metaphase ($n = 20$), and anaphase ($n = 38$) with an average distance of 3.6 ± 1.2 μm SD and angular orientation of 73.5° ± 44.3° SD, 3.3 ± 1.8 μm SD and 82.4° ± 50.9° SD, and 2.9 ± 1.4 μm SD and 88.4° ± 50.1° SD, respectively. The blue asterisk indicates a measurement representative of homologous chromosome pairing. (*F*) A connected scatterplot portraying the relative frequency distribution of minimal distance between chromosome 4 and its homologous partner (green line) or a nonhomologous chromosome (chromosome X or Y, gray dotted lines) at metaphase (square)/anaphase (triangle) ($P = 0.030$, $P < 0.001$ for metaphase/anaphase). (*G*–*J*) Select frames of a high-resolution 4D time-lapse movie of a cell labeled with CENP-A GFP and centrin1-GFP (arrowheads) to visualize the centromeres and centrosomes, respectively, undergoing mitosis from a top view (*G*–*J*) or a side view (*G*′–*J*′). Six centromeres are labeled (colored spots) at an initial time point at (*G* and *G*′) prometaphase and tracked (colored lines) until metaphase (*H* and *H*′). Other centromere tracks are designated in gray. Note that at the beginning of prometaphase the centrosomes are above/below the chromosome rosette. (*I* and *I*′) As in *H* and *H*′ but from metaphase to anaphase. (*J* and *J*′) As in *H* and *H*′ but from anaphase to telophase. (*K*–*K*″) Tilted view of a HUVEC at anaphase stained with DAPI (blue) and γ-tubulin (white) visualized by immunofluorescence with the center of mass of the two sister anaphase chromosome masses labeled (white pixels) from confocal optical sections. Note that the centrosome, or mitotic spindle, axis is coincident with a nuclear meridional plane in mitotic cells. (*K*′) top view. (*K*″) side view. (*L*) Schematic delineating the *x*, *y*, and *z* axes in a cell at anaphase. The *x* axis was determined by the line crossing the center of mass of the two sister anaphase chromosome masses, the *z* axis was determined as the perpendicular line to the coverslip, and the *y* axis was defined as perpendicular to both *x* and *z* axes. (Scale bars: 1 μm.)

autosome pairs exhibited angular measurements of <90° (*SI Appendix*, Fig. S1*A*), indicating the homologous chromosomes deviated from a theoretically defined antiparallel configuration. A rose plot, displaying the frequency of angular distribution for the different homologous chromosomes, shows high angular variations ($n = 37$, χ^2 test $\chi^2 = 0.10$; *SI Appendix*, Fig. S1*A*). Thus, the data are not consistent with the antiparallel/fixed position model for individual homologous pairs.

In no case, however, did we find two homologs occupying the same position within a prometaphase rosette. For example, for chromosome 4 each homolog was consistently separated from one another with an average distance of 3.6 ± 1.2 μm SD ($n = 12$/12 cells; Fig. 1 *D* and *E*). Our data also suggest that homologous pairs are not completely positioned at random. Instead, they hint at the existence of an unknown mechanism(s) that restricts spatial proximity between homologs in mitotic cells. To test this possibility, we examined the spatial organization of homologs in the subsequent mitotic stages. A pair of homologous chromosomes continued to be spatially segregated at metaphase ($n = 20$/20 cells; Fig. 1 *B*, *E*, and *F*) and anaphase ($n = 38$/38 cells; Fig. 1

C, *E*, and *F*) (null hypothesis: homologs positioned at random relative to each other and similar to a nonhomologous partner, Student's *t* test, $P = 0.030$, $P < 0.001$, for metaphase/anaphase; Fig. 1*F*). These data demonstrate that homologous chromosomes are not organized in an antiparallel orientation to each other. However, they did not come into contact and did appear to segregate from one another, thus being antipaired in fashion, throughout mitosis.

The above findings—that homologous chromosomes are predominantly distant from each other and not often close at different stages of mitosis—prompted us to question whether this reflects a level of organization in the mitotic chromosomes and/or overall cellular organization. With the emergence of new tools and the ability to define axes in 3D with cellular markers, it is now possible to accurately map the positions of individual chromosomes along a subcellular axis/plane. To develop and validate a 3D coordinate system to reliably map the homologs, the extent of chromosome movement, such as translational/rotational movements, was determined and the *x*, *y*, and *z* axes were defined during mitosis.

We tracked and analyzed the position and movement of individual chromosomes throughout mitosis in real time, using a human epithelial cell line (RPE1) (19) that stably expresses CENPA-GFP and centrin1-GFP to identify the centromeres/chromosomes and centrosomes/nuclear division axis, respectively. The 3D, live-cell analysis revealed that from prometaphase to metaphase chromosomes displayed unstable movements along the centrosome axis ($n = 5$; Fig. 1 *G–H* and Movie S1), most likely due to concurrent formation of the mitotic spindle (27). In contrast, from metaphase to anaphase chromosomes exhibited stable movements along the nuclear division axis ($n = 14$; Fig. 1 *I* and *I′* and Movie S2). Individual chromosomes predominantly moved parallel to, or along, the centrosome axis with little perpendicular fluctuation. Perpendicular fluctuation and rotation of chromosomes along the centrosome axis became apparent following late anaphase ($n = 7$; Fig. 1 *J* and *J′* and Movie S3). As the nuclear envelope reforms during telophase, chromosomes in the sister nuclei act independently and asynchronously (Movie S3). The small displacement changes from metaphase to early anaphase suggested that individual chromosomes maintained their relative position to another and within the mitotic chromosome mass. These results also corroborate previous studies showing limited movements when chromosomes are attached to the mitotic spindle (19, 27, 28). Therefore, the absence of major displacement changes at metaphase to midanaphase allowed us to quantitatively map individual chromosomes in a 3D coordinate system (Fig. 1 *K–L*). The *z* axis was fixed as the optical path of the microscope, a perpendicular line to the coverslip, and along the apical–basal axis. The *x* axis is perpendicular to the *z* axis and coincident with the centrosome axis (Fig. 1 *K*, *K′*, and *K″*); the origin (0, 0, 0) was then defined by a line crossing the center of the mitotic chromosomal mass, and the *y* axis was defined as perpendicular to both *x* and *z* axes (Fig. 1*L*). At prometaphase, a lack of a definable *y* axis along the plane of the chromosome rosette prevented establishment of a coordinate system.

To test whether there was a conserved position/address for each pair of homologous chromosomes that could be responsible for the antipairing organization of homologs we systematically mapped individual chromosomes in a 3D axial coordinate system (*SI Appendix*, Fig. S2 *A–E*). We quantified chromosome position using both 3D, superimposed, homolog contour map data and a normalized 2D axial coordinate system (*SI Appendix*, Fig. S2 *F–I*). The summation of all homologous chromosomes in physical space was plotted on a 3D contour map, upon which grayscale saturation represents the density of localization when all of the homologous chromosomes are overlaid (*SI Appendix*, Fig. S2 *F* and *H*). Isolines were then generated that connect contours that share the same gray value/intensity, revealing hotspots of maximal overlap. If the homologous chromosomes were in fixed positions there would be a clustered area of high density/occurrence that reflects the colocalization frequency for each of the homologs. In addition, the mapped position of each homologous pair in a coordinate system would also be identical for every cell. Neither analysis identified any evidence of fixed localizations for the homologous chromosomes based on the coordinate system in the present study (*SI Appendix*, Fig. S2 *F–I* and Movie S4). However, there was a modest correlation of chromosome size to position based on median values for individual chromosome populations ($n = 578$ cells, $R^2 = 0.6119$, $P < 0.05$; *SI Appendix*, Fig. S1*J*), corroborating previous work (29). These results suggest an alternative mechanism that is not regulated by a defined address that drives the antipairing organization of homologs.

Homologous and XY Chromosomes Segregate to Opposite Nuclear Hemispheres During Mitosis. Although our superimposed 3D matrix analysis demonstrated that a pair of homologs does not display fixed positions, surprisingly a distinct pattern did emerge. The 3D overlay data revealed that each autosome in a pair was localized to separate hemispheres, on either side of a "meridional plane" ($n = 15/20$ metaphase cells and $n = 28/38$ anaphase cells, Fig. 2 *A* and *B* for chromosome 4; see *SI Appendix*, Fig. S3 *A–AR* for all other autosomes). The meridional plane, an imaginary *xz* plane horizontal to the metaphase/anaphase equatorial plate, was coincident with the centrosome, or *x*, axis, and was found to traverse along the apical/basal, or *z*, axis ($n = 28$ cells; Fig. 1 *K–L*). Midpoint calculation for pairs of homologous chromosomes confirms the meridional plane to consistently partition individual homologs to separate hemispheres (Fig. 2*C*). To test whether such an arrangement occurs by random chance, a statistical binomial test (30, 31) was performed on the positional coordinates of the center of mass for each chromosome ($P = 0.021$, $P = 0.003$ at metaphase/anaphase) (null hypothesis: homologous chromosomes are randomly arranged in the two nuclear hemispheres). The data support the presence of an axis-dependent antipaired configuration of one homolog per nuclear hemisphere at metaphase that persists throughout anaphase in dividing cells.

To evaluate whether sex chromosomes followed the same patterning observed for autosomes, female-derived HUVECs were examined with X chromosome-specific probes at metaphase and anaphase (*SI Appendix*, Fig. S3 *AS–AX*). The pair of X chromosomes showed the identical one homologous partner per hemisphere motif, rather than a random or overlapping distribution ($n = 18/24$ metaphase cells, $P = 0.011$ and $n = 32/42$ anaphase cells, $P = 0.001$; *SI Appendix*, Fig. S3 *AS–AX*). To explore whether the idea of a sequence homology based-repulsion between a pair of homologs is required for this organization, we visualized the sex chromosomes in male cells as each partner has minimal levels of sequence homology (32). The X and Y chromosome preserved the same pattern of one homolog per hemisphere in male cells ($n = 19/28$ metaphase cells, $P = 0.044$ and $n = 20/28$ anaphase cells, $P = 0.001$; Fig. 2 *D–F* and Movie S5). This result suggests that sequence homology is not required for establishing the one-homolog-per-hemisphere motif. Simultaneous visualization of sex and autosomal chromosomes demonstrates that both XY and homologous pairs follow the same topological hemisphere segregation (Fig. 2 *G* and *H*). Consequently, this discrete chromosomal organization produces a compartmentalization of two complete haploid chromosome sets along the nuclear division axis. In addition, another primary human cell type displayed a similar haploid set segregation motif (human fibroblasts, HFFs; *SI Appendix*, Fig. S4 *A–F*), suggesting the pattern may be conserved broadly for multiple cell types and is cell-type-independent.

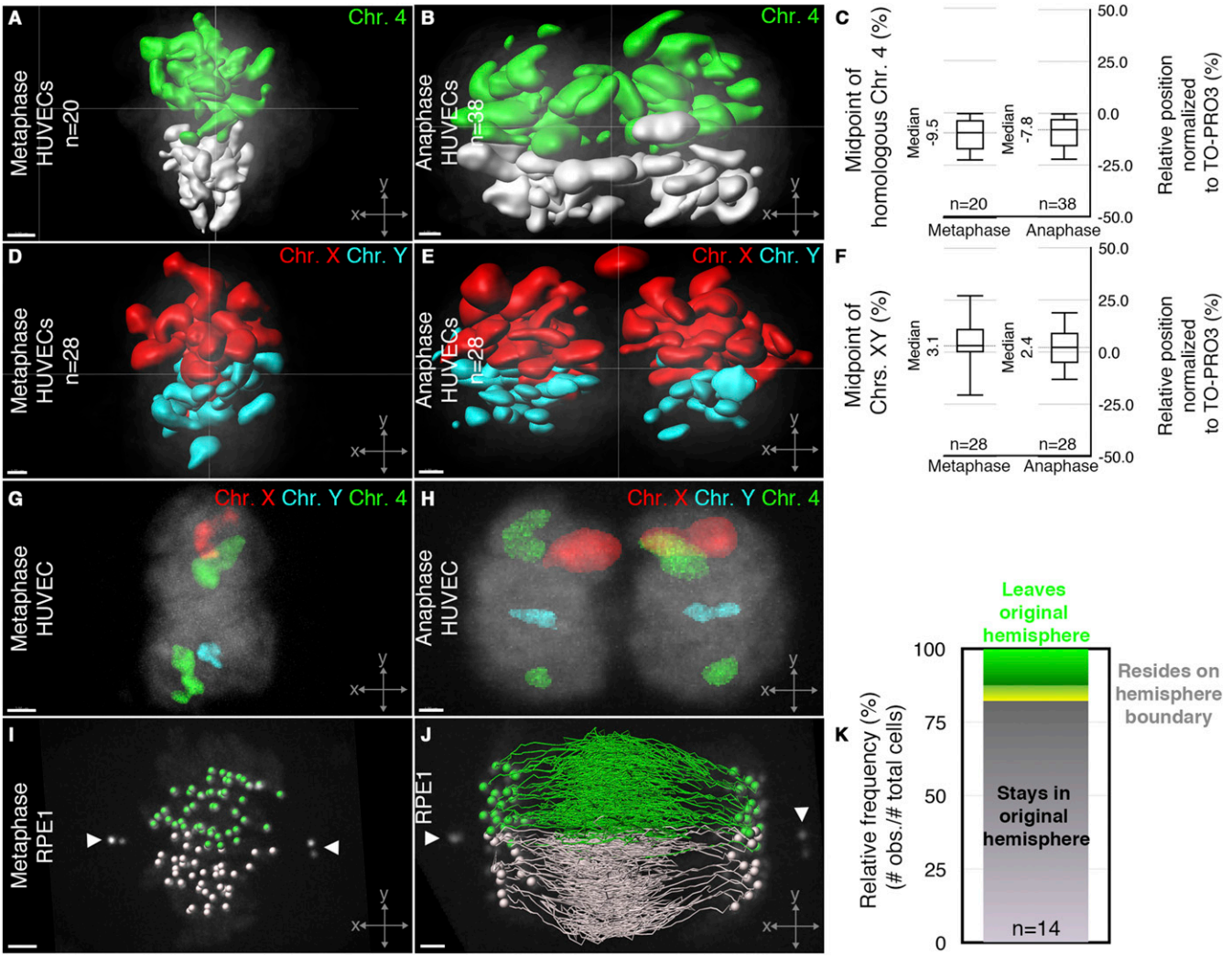

Fig. 2. Homologous and XY chromosomes segregate to opposite nuclear hemispheres during mitosis. (*A*) Top view of a 3D overlay of chromosome 4 (green/white) distribution of multiple HUVECs at metaphase stained with TO-PRO3 (gray) ($n = 20$). Each homologous chromosome 4 of a pair was assigned to be either green or white based on its proximity to the *y* axis, when $y = 0$ (green was assigned to most proximal, and white the most distal) and mapped to generate 3D overlay data. The *x* and *z* axes are the same as in Fig. 1*L*, with the *y* axis defined as a line crossing the furthest edges of the metaphase plate. (*B*) As in *A* but at anaphase ($n = 38$). (*C*) A box plot summarizing the median of midpoint values of homologous chromosome 4 pairs at metaphase and anaphase. (*D–F*) As in *A–C* but of chromosome X (red) and Y (cyan) of male-derived HUVECs ($n = 28$ nuclei). As no directionality of individual chromosome pairs along the *y* axis can be predetermined, all X chromosomes were given a positive value along the *y* axis. (*G*) Top view of a HUVEC at metaphase stained with TO-PRO3 (gray) and painted for chromosome 4 (green), X (red), and Y (cyan) from confocal optical sections. (*H*) As in *G* but at anaphase. (*I* and *J*) Top view of a high-resolution 4D time-lapse movie of a cell labeled with CENP-A GFP and centrin1-GFP (arrowheads) with two groups of individual centromeres labeled (green/white spots) at metaphase (*I*) and tracked (green/white lines) to midanaphase (*J*). (*K*) Quantification of individual centromere retention in original nuclear hemisphere from metaphase to midanaphase ($n = 14$). (Scale bars: 1 μm.)

Consistent with these observations, when chromosomes were assigned to groups based on their initial start position along the centrosome axis at metaphase and tracked to anaphase using the CENP-A/centrin1-GFP cell line, we found minimal mixing of individual chromosomes between the two groups (Fig. 2 *I* and *J* and Movie S6). Detailed quantification of chromosomes at the interface between the two labeled groups demonstrates that the majority of chromosomes remain largely in their original positions relative to the chromosome mass (Fig. 2*K*). The data conclude that, in the absence of major chromosome fluctuations perpendicular to the centrosome axis during mitosis, the axis-dependent segregation between a pair of homologous chromosomes is conserved from metaphase to anaphase. These results thus confirm that the sets of chromosomes are showing a collective behavior during mitosis and support that collective genome segregation occurs as a haploid set.

A possible mechanism underlying the haploid set-based segregation is that each haploid compartment contains chromosomes of the same parental origin. Since the male and female pronuclei do not immediately fuse and are separated at early stages after fertilization (21, 33–39), it is plausible this parental origin may be spatially inherited as the identity for each haploid set. In support of this parental origin hypothesis, we tested two different experimental conditions: (*i*) Compartmentalization of a haploid chromosome set is spatially preserved in naturally occurring tetraploid cells (4n), and (*ii*) genetic tracing of chromosomes reveals haploid set derived by parental origin.

Haploid Set Compartmentalization Is Conserved in Naturally Occurring Tetraploid Cells (4n). To first test whether a haploid set compartmentalization is spatially preserved and tightly regulated, we took advantage of naturally occurring tetraploid cells

(4n) in human primary culture that undergo a whole-genome duplication event (40, 41). If individual haploid chromosome sets are sequestered from each other, we might expect this motif would be preserved following an additional duplication without nuclear separation in normal cells. We examined the sex chromosome distribution of male tetraploid HUVECs during mitosis to test whether tetraploid cells maintained compartmentalization for each of the four haploid sets (karyotype: XXYY). From prometaphase to anaphase, all of the four individual sex chromosomes were segregated from each other (n = 4/4 prometaphase cells, n = 16/20 metaphase cells, and n = 8/10 anaphase cells; Fig. 3 *A*–*C*). Quantitation of the distance and angular orientation of the XX and YY sex chromosome pairs revealed no pairing/overlap between the identical chromosome pairs within a tetraploid cell (n = 19/20 metaphase cells; Fig. 3*D*). Surprisingly, 3D overlay data showed each sex chromosome segregated to separate quadraspheres along an axis parallel to the meridional plane (n = 15/20 cells; Fig. 3*E*). When the distance between both XY pairs in a single tetraploid cell was compared by subtraction, with zero representing identical distances, approximately similar distances for XY pairs were found with an average distance of 1.2 ± 1.1 μm SD (n = 20 cells; Fig. 3*F*). Taken together, these data suggest the compartmentalization of four individual haploid sets (1n) in tetraploid cells (4n) along the nuclear division plane (Fig. 3*G*). The data are not only consistent with previous findings of haploid set separation in triploid cells (9, 42) but also with the parental origin model, in which each haploid set is spatially discrete and compartmentalized.

In Vitro and in Vivo Segregation of Mouse Chromosomes. To directly test whether each haploid set is derived by parental origin, we labeled the maternal genome using a translocation mouse, Ts65Dn (43–47), which produces an extra supernumerary marker chromosome, to genetically distinguish the maternal genome set from the paternal genome set (Fig. 4*G*). However, first we had to determine whether homologous chromosomes in the mouse share the same haploid set-based antipairing organization as in humans. Our chromosome paint assessment of primary mouse embryo-derived fibroblast cells (MEFs) confirmed that, similar to humans, the homologs are not paired and segregated to separate hemispheres (n = 28/36 anaphase cells, P = 0.001; Fig. 4 *A*–*D*). The sex chromosomes also displayed the one-homolog-per-hemisphere motif (n = 28/42 cells, P = 0.022; Fig. 4 *E* and *F*). Taken together, these results demonstrate the haploid set-based pattern is conserved in the mouse.

The translocated chromosome 17^{16} was distinguished from intact chromosome 16 by its size in anaphase cells (Fig. 4*H*). Each homologous chromosome 16 localized separately to either nuclear hemisphere, one of which contained the translocation chromosome 17^{16} (n = 28/42 cells, P = 0.022; *SI Appendix*, Fig. S5 *A* and *B*). To identify which X-, or Y-containing haploid set was most likely associated with the translocation chromosome, we first determined the approximate boundary between the haploid sets by finding the midpoint of the pair of homologous chromosome 16. We then mapped the position of the translocated chromosome (Fig. 4*L*). In the majority of cases we examined, the hemisphere containing the translocated chromosome 17^{16} also

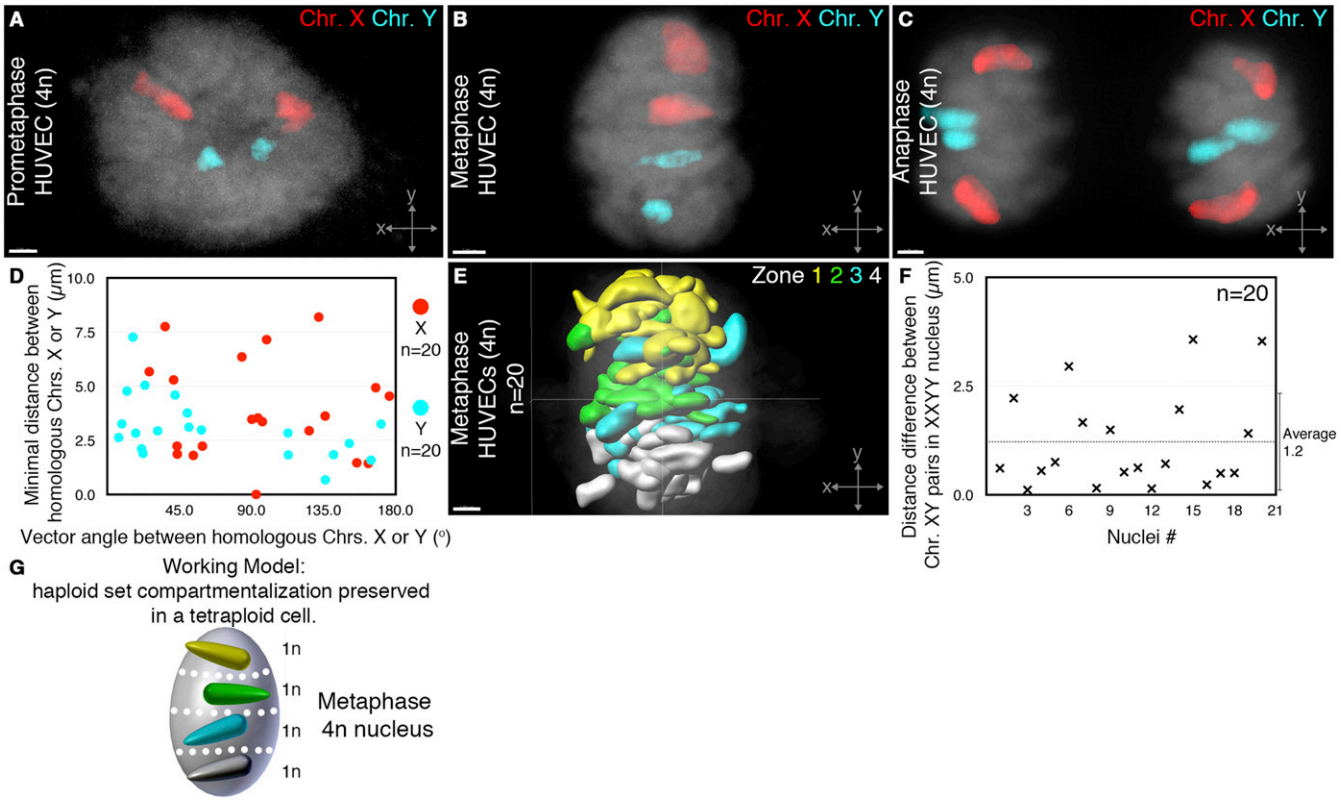

Fig. 3. Haploid set compartmentalization is conserved in normally occurring tetraploid (4n) cells. (*A*) Top view of male tetraploid (XXYY) HUVEC at prometaphase stained with TO-PRO3 (gray) and painted for the X (red) and Y (cyan) chromosome. (*B* and *C*) As in *A* but at metaphase and anaphase, respectively. (*D*) Distance and angular orientation of the XX and YY sex chromosome pairs (n = 19/20 cells at metaphase) with an average distance of 3.9 ± 2.3 μm SD and 3.1 ± 1.26 μm SD and angular orientation of 95.9° ± 47.9° SD and 68.3° ± 58.5° SD, respectively. (*E*) A 3D overlay of sex chromosome distribution of multiple male tetraploid (XXYY) cells at metaphase (n = 20). Each sex chromosome, X or Y, was assigned to be yellow/green/cyan/white based on its sequential order along the *y* axis and mapped to generate 3D overlay data. (*F*) Distance differences for a pair of XY chromosomes between two nuclear hemispheres with mean and SD error bars (n = 20). (*G*) Model for haploid set compartmentalization in a tetraploid cell. (Scale bars: 1 μm.)

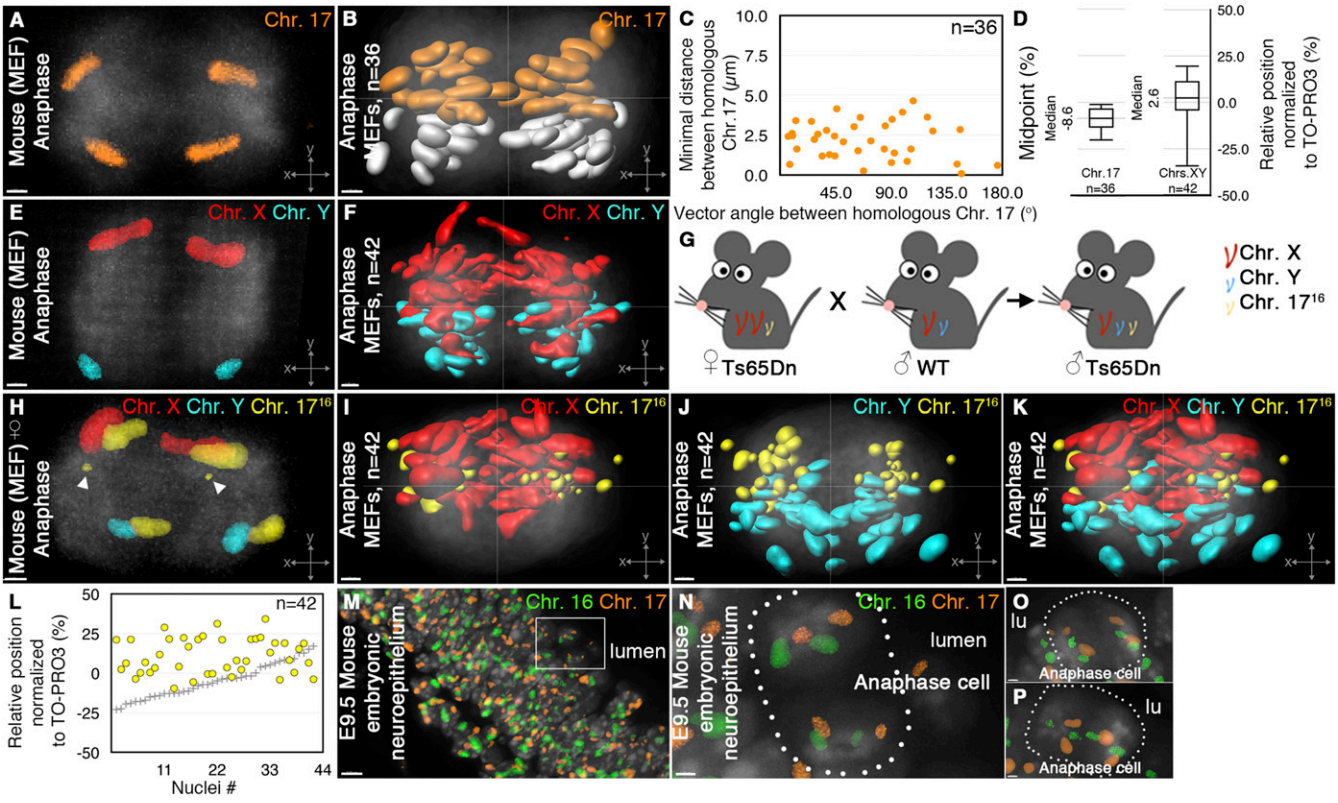

Fig. 4. In vitro and in vivo segregation of mouse chromosomes. A maternally derived supernumerary chromosome segregates with the X chromosome. (*A*) Top view of a cell at anaphase of primary WT MEFs stained with TO-PRO3 (gray) and painted for chromosome 17 (orange). (*B*) A 3D overlay of chromosome 17 (orange/white) distribution of multiple cells at anaphase ($n = 36$), (*C*) with an average distance of 2.2 ± 1.2 μm SD, and angular orientation of 68.9° ± 45.5° SD. (*D*) A box plot presenting the midpoint median values for a pair of homologous chromosome 17 and the XY chromosome data points at anaphase. (*E* and *F*) As in *A* and *B* but of chromosome X (red) and Y (cyan) of male-derived MEFs ($n = 42$). (*G*) Mating strategy for using the Ts65Dn mouse to genetically distinguish the maternal genome set from the paternal genome set. (*H–K*) As in *E* and *F* but of primary MEFs for the male Ts65Dn progeny from a Ts65Dn maternal/WT paternal genetic cross, painted additionally with chromosome 16 (yellow) and the translocated chromosome 17^{16} (yellow with arrowheads). Note that the translocated chromosome 17^{16} is identified by its small size. (*L*) Relative position for each translocated chromosome 17^{16} (yellow circles) and the midpoint of a pair of homologous chromosome 16 (+) in the same cell was determined for the male Ts65Dn progeny from a Ts65Dn maternal/WT paternal genetic cross ($n = 42$). The X- or Y-containing hemisphere domains are defined as being above/below the plus sign (+), respectively. (*M*) A longitudinal section of a E9.5 male embryonic neuronal lumen painted for chromosome 16 (green) and 17 (orange) and stained for nuclei with DAPI (gray). (*N*) A neuroepithelial anaphase cell (dotted line) (the boxed area in *M*) shows segregation of homologous chromosomes 16 and 17. (*O* and *P*) As in *N* but of other examples. (Scale bars: 1 μm; 5 μm in *M*.)

contained the maternally derived X chromosome ($n = 28/42$ cells, $P = 0.022$; Fig. 4 *H–L* and Movie S7). If the 17^{16} chromosome behaves similarly to other wild-type autosomes, these results are consistent with the model wherein one haploid set of an individual cell contains the maternally derived chromosomes while the other haploid set contains the paternally derived chromosomes.

To address whether the antipairing organization of homologs seen in cultured cells reflects the chromosome organization in their physiological environment, we examined the distribution of homologous chromosomes in neuroepithelial cells of E9.5 mouse embryos. Analyses of anaphase cells revealed consistent separation of homologs ($n = 22/28$ cells; Fig. 4 *M–P*), in accord with cultured cells (Figs. 1–4). These data indicate that the establishment and maintenance of separation for homologous chromosomes are also conserved in the embryo.

Discussion

Genomes are dynamic entities that can be changed by processes such as recombination (1–3). As genome complexity increases, recombination events during mitosis minimize and are limited to meiosis (48). Therefore, homologous recombination must be tightly regulated to avoid genomic instability at mitosis but allow for precisely programmed genetic diversity during meiotic differentiation (49).

Our study has demonstrated a haploid chromosome set-based antipairing organization of homologous chromosomes during mitosis in human cells. A previous study has shown that translocations can occur independently of cell cycle stage through experimental induction (50), therefore suggesting the presence of a mechanism during mitosis to limit DNA exchange. Notably, direct evidence for the antipairing principle is supported by high-throughput screens that have elucidated candidate genes that antagonize somatic homologous pairing in the fly (51, 52). Spatial segregation of two haploid chromosome sets to discrete nuclear hemispheres may function to keep individual homologous partners apart, preventing, or at least minimizing, allelic misregulation and/or genetic recombination in complex genomes during mitosis. The purpose of this antipairing was indirectly tested when we observed a cancer cell line (53), which exhibited abnormal homologous pairing and consequently lost the haploid set-based antipairing pattern (Fig. 5).

How the haploid set-based groupings emerge still remains an interesting question yet to be answered. Although our data support the paradigm (13, 14, 47) that haploid sets are derived by parental origin, there are limitations to our analysis. The

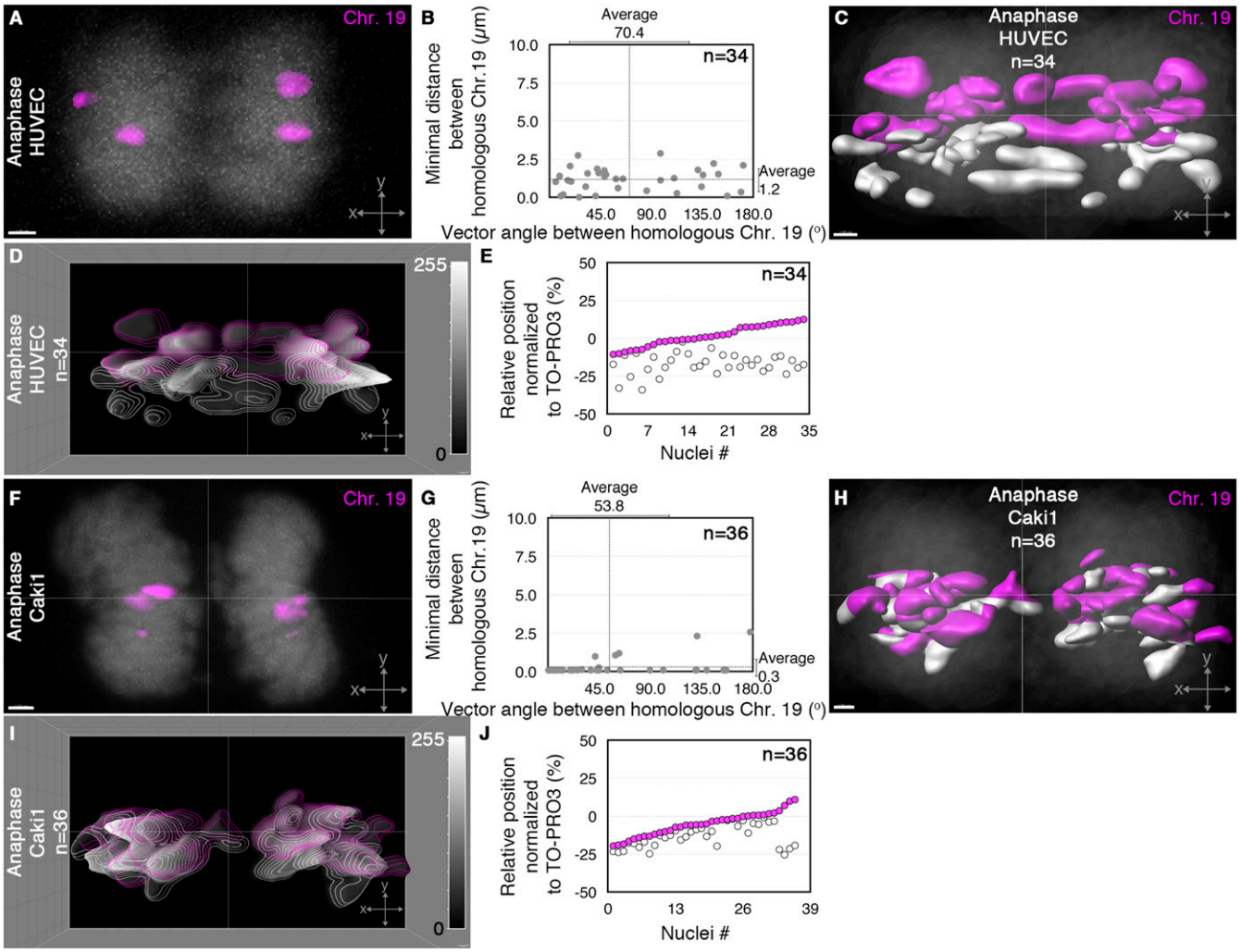

Fig. 5. The one homologous chromosome per nuclear hemisphere pattern is lost in a cancer cell line. (*A*) Top view of a HUVEC at anaphase stained with TO-PRO3 (gray) and painted for chromosome 19 (magenta) from confocal optical sections. (*B*) Distance and angular orientation of homologous chromosome 19 pairs ($n = 34$ nuclei) with an average distance of 1.2 ± 0.8 μm SD and angular orientation of 70.4° ± 52.0° SD. (*C*) Top view of a 3D overlay of chromosome 19 (magenta/white) distribution of multiple cells at anaphase ($n = 34$). (*D*) A 3D superimposed contour map of chromosome 19 (magenta/white isolines) at anaphase of HUVECs ($n = 34$). (*E*) Relative positions for each pair of homologous chromosome 19 (magenta/white circle) when mapped to an axial coordinate system ($n = 34$) (defined in Fig. 1*K*). Other conditions were as in *SI Appendix*, Fig. S2. (*F–J*) As in *A–E* but of renal carcinoma cells (Caki1) ($n = 36$) with an average distance of 0.3 ± 0.6 μm SD and angular orientation of 53.8° ± 52.6° SD. Note that Caki1 cancer cells exhibit higher-frequency pairing of homologous chromosome 19. (Scale bars: 1 μm.)

reciprocal genetic cross with the Ts65Dn male mice to follow the paternally derived supernumerary chromosome proved to be challenging, as they are sterile (5, 54). However, a selective breeding of rare fertile males for unknown reasons were identified (55). The paternally derived translocation chromosome localized to the boundary between two nuclear hemispheres, making it difficult to determine its association to either X- or Y-containing hemispheres (*SI Appendix*, Fig. S5 *C–I*). Our study does not rule out the possibility that the supernumerary chromosome does not behave like a wild-type autosome, as it lacks a homologous partner. These rare fertile Ts65Dn male mice may be genetically unstable and exhibit chromosome characteristics more in common with diseased states such as cancer rather than native/endogenous cells. It is intriguing that both the paternally derived supernumerary chromosome (*SI Appendix*, Fig. S5 *H* and *I*), and paired homologous chromosomes in cancer cells (Fig. 5 *I* and *J*) are nonrandomly positioned along the boundary between the nuclear hemispheres.

Genome-wide 3D proximity maps and DNA FISH analyses at interphase (G_0/G_1) have shown a low frequency of interaction between homologs (56–58). These previous studies hint that the haploid set-based antipairing segregation may also be present at interphase, although homologs have been found to come in contact after induction of DNA damage in nonproliferative cells (59). We therefore examined whether the two haploid chromosome sets remain spatially distinct at interphase. However, interphase nuclei often rotate in a variety of cell types (60–62), which may complicate interpretation of chromosome mapping data. To avoid such complexity we examined monocytes, which allowed us to assign decondensed chromosome location along the longitudinal axis of a horseshoe-shaped, interphase nucleus (*SI Appendix*, Fig. S4 *G* and *H*). Three-dimensional overlays showed that both homologous autosomes and XY chromosomes did not segregate to separate nuclear halves (*SI Appendix*, Fig. S4 *G* and *H*). Although our chromosome paint approach is not effective in complete euchromatin detection, the above data suggest

that interphase monocyte nuclei lack a clear hemisphere-based haploid separation.

Another technical limitation/challenge in testing our haploid set-based segregation model in mesenchymal cells is due to the lack of apparent polarity that prevents application of our coordinate system to accurately map chromosome positions between cells. In the future, it would be necessary to reevaluate chromosome mapping in mesenchymal cells including mouse ES cells (25) and immortalized nonepithelial cell lines.

Many possible mechanisms can be implicated for this haploid set chromosome sequestration. These include intrinsic chromosome identity, such as preexisting parental identity of haploid sets, and/or cytoskeletal components to sequester one haploid chromosome set from the other while keeping both sets together without nuclear fragmentation. A recent paper has shown involvement of the cytoskeleton in parental genome segregation at fertilization (26). Although this paper attributes the parental genome segregation to the two mitotic spindles which disappear after the eight-cell stage, it would be interesting to interrogate other cytoskeletal factors that may persist to regulate haploid set segregation. What underlying mechanism(s) must exist for one haploid set to encompass all autosomes and one sex chromosome, however, still remains to be explored. Our study reinforces/renews a foundation to further explore a conserved mechanism in mitotic cells that sequesters haploid chromosome sets along a subcellular axis for antipairing.

Materials and Methods

Cell Preparation and Culture. Primary mouse embryonic fibroblasts were established from harvested E13.5 embryos (63) as described. HUVEC cells (PCS-100-013; ATTC) were cultured in MCDB-131 complete media (Life Technologies) supplemented with LVES (Life Technologies), 1% penicillin-streptomycin, and 1% L-glutamine. Human foreskin fibroblasts (CCLZR211; UCSF Cell Culture Core Facility) were cultured in DMEM H-21 media supplemented with 10% FBS, 1% penicillin–streptomycin, and 1% L-glutamine. The human epithelial cell line (CENP-A/centrin1-GFP RPE1) (24) was a gift from Alexey Khodjakov, New York State Department of Health, Albany, NY. CENP-A/centrin1-GFP RPE1 cells were cultured in DMEM/F12 (1:1) media supplemented with 10% FBS and 1% penicillin–streptomycin. All cells were cultured in a 37 °C incubator in a 10% CO_2 atmosphere. For high-resolution imaging, cells were grown on custom diagnostic slides with 8-mm fields (Azerscientific) to 75–80% confluence. Human CD14+ monocytes (PB011; All Cells) were immediately spun down using a Cytospin (Shandon 4; Thermo Scientific) onto Superfrost slides (Fisher Scientific) for use.

Mouse Lines and Genotyping. Female Ts65Dn translocation mice (4–8) and wild-type mice (C57BL/6J) were both purchased from The Jackson Laboratories. Rare male Ts65Dn (55) translocation mice were a gift from Roger Reeves, Johns Hopkins University, Baltimore. Female/male Ts65Dn mice or wild-type mice were crossed to male/female wild-type mice to generate F1 embryos for collection at E9.5 and E13.5. Genotyping for the chromosome translocation and determination for embryonic sex was employed using PCR on purified genomic DNA obtained from yolk sac samples using previously reported primers (64, 65). All animal protocols were approved by the University of California, San Francisco Institutional Animal Care and Use Committee and in agreement with all institutional and federal guidelines.

Fluorescence in Situ Hybridization. HUVECs, HFFs, and MEFs were grown on slides, and human monocytes were spun down on slides for chromosome painting/DNA-FISH as previously described (63). Mouse embryos were fixed at E9.5 with freshly made 4% paraformaldehyde diluted in PBS, pH 7.4. Preparation for embryonic cryosections was performed as described with modifications to the antigen retrieval step using 10 mM NaCitrate, pH 6 (66). Slides were then processed with the continuation of the ethanol series referenced in the above method (63). Slides were denatured/codenatured with Whole Chromosome Paint probes (Applied Spectral Imaging) at 80 °C with 70% formamide/2× SSC for 5 min (for HUVECs/HFFs/human monocytes), 7.5 min (MEFs), or 12 min (E9.5 embryonic mouse cryosections).

Immunofluorescence. HUVECs were grown on slides, fixed with ice-cold −20 °C 100% methanol for 5 min at −20 °C, rinsed three times with cold PBS, and incubated with permeabilization solution (PFS) (0.7% fish skin gelatin, 0.025% saponin dissolved in PBS) for 1 h at room temperature (RT). Slides were then incubated with primary antibodies to rabbit γ-tubulin (1:1,000, T5326-200UL; Sigma) and DAPI (1:1,000) diluted in PFS for 1.5 h at RT, washed four times for 5 min each with PFS at RT, and incubated with secondary antibodies to goat anti-rabbit IgG Alexa Fluor 488 (Invitrogen) for 1 h at RT. Final washing was completed at RT with PFS four times for 5 min each and PBS three times for 5 min each then mounted with Prolong Antifade (Invitrogen).

Image Capture and Acquisition. Fixed mitotic cells were imaged with a confocal microscope (TCS SP2; Leica) using a 63× oil immersion objective with a digital 2× zoom. The image data were captured sequentially in a multitrack, four-channel mode. The Z-stacks were acquired using a frame size of 1,024 × 1,024 with a two-frame average and processed with Leica Application Suite (Advanced Fluorescence Lite 2.3.5 build 5379 software).

For high-resolution live imaging, cells were grown on 35-mm glass-bottom dishes (Ibidi). Cells were then placed in an incubation chamber (Okolab enclosure and Bold line incubator) on the motorized microscope stage (Piezo Z-drive) at 37 °C under a 10% CO_2 atmosphere and imaged with a inverted fluorescence microscope (Nikon Ti) attached to a spinning disk confocal (CSU-22) using a Plan Apo VC 100×/1.4 oil immersion objective. The image data were captured in a single-channel mode. The Z-stacks were acquired using a frame size of 512 × 512 every 10 s for an hour with an electron-multiplying CCD camera (Evolve Delta; Photometrics) and processed with Nikon Elements (4.5 build). CENP-A/centrin1-GFP was excited with a 488-nm laser (150-mW Coherent OBIS). Brightness and color were adjusted using Photoshop (Adobe Systems).

Mitotic Cell Selection for Fixed Cell Analysis. Prometaphase rosettes/cells which displayed an unbroken radial, symmetrical configuration of chromosomes and a centrally located DNA-deficient zone (an absence of TO-PRO3 signal) were analyzed. Rosettes that were asymmetrical, or displayed a distorted shape, were not included in the analysis due to regional variations in DNA condensation within the cell (67). Inclusion of these variations could thus lead to skewed measurements in favor of homologous chromosome randomization. Metaphase cells were identified by linearly aligned chromosomes characteristic of this cell cycle stage (32, 68). Early/mid anaphase cells were identified by incomplete nuclear division (contiguous TO-PRO3 signal between two sister chromosome masses), and by an absence of a constriction characteristic for cytokinesis during late anaphase (69). Typically 0.02% of cells were in early/mid anaphase under our culture conditions. For example, for one experimental group of HUVECs, of 56,547 cells examined 11 mitotic cells were in early/mid anaphase. In contrast, telophase cells were identified by the presence of cellular constriction at the middle of the cell (69).

We chose not to use cell lines for our homologous chromosome mapping analysis, which can generate chromosomal abnormalities including aneuploidy (70–72), or cell cycle synchronization methods. Synchronization drugs have been reported to interfere with native chromosome associations (73) and therefore could impact chromosome positioning. Therefore, despite the increase in numbers of mitotic cells this would yield, we did not want to compromise the data by introducing a potential confounding artifact into the system.

Three-Dimensional Angular Measurements to Test for Antiparallel Configuration at Prometaphase. Our time-lapse imaging movies tracking centromere movement throughout mitosis demonstrate that centromeres exhibit less mobility than the chromosome arms (Movies S1–S3). Therefore, to determine whether homologous chromosomes were arranged in an antiparallel configuration for prometaphase rosettes/cells, the closest point for each homolog to the center of the rosette was used to more accurately/precisely map individual homolog position. This closest point was used to represent the estimated centromeric region for each chromosome. Centromeric sequences are shared between nonhomologous chromosomes (74, 75). Therefore, due to the specificity of chromosome paints, centromeres were not individually labeled. Three-dimensional angular measurements for homologous chromosomes were then calculated/determined using these individual points and the center of the rosette.

Three-Dimensional Distance and Angular Orientation Measurements. Interhomologous distances were determined by using edge-to-edge measurements between chromosome paint signals. The edge-to-edge, or minimum, distance is defined as the shortest 3D distance between the boundaries/borders of a homologous pair determined by the two closest voxels of the two homologous chromosomes. Computation of interhomologous angles was

performed by finding the angle between two vectors. A vector was defined as the longest axis of an ellipsoid contained within each homologous chromosome. Therefore, a homologous pair was identified as being paired if the distance was ≤0.36 μm, the spatial resolution limit, and angular orientation = 0°.

Three-Dimensional Centromere Tracking of Time-Lapse Analysis. For live-cell analysis, sample drift correction (translational) was performed computationally for each cell by using the fixed *z* axis defined by the laser line and the centrosome axis as reference points. Three-dimensional centromere movements were analyzed using Imaris software (spot object tracking algorithm) to track individual centromere trajectories over time. Spots were defined by CENP-A GFP signal as 0.5 μm in diameter. A minority of spots (~10%) that overlapped and/or had low signal due to fluorophore bleaching over time were not included in the centromere trajectory analysis.

Three-Dimensional Reconstruction and Overlay for Fixed Cell Analysis. Mitotic cells were individually cropped in each optical section and reconstructed into 3D and analyzed using Imaris software (Bitplane). For fixed cell analysis fluorescent images were thresholded by highlighting the brightest 50% of the image for all channels. Three-dimensional surfaces were then rendered and center of mass for each homologous chromosome was determined.

For 3D overlays, the position of center of mass of homologous chromosomes was mapped to a 3D axial coordinate system for metaphase/anaphase cells. The *y* axis was defined as a line crossing the furthest edges of the metaphase plate, the *z* axis was determined as the perpendicular line to the coverslip, and the *x* axis was defined as perpendicular to both *y* and *z* axes. For anaphase cells, the 3D axial coordinate system (Fig. 1*L* and *SI Appendix*, Fig. S2 *A*–*E*) was defined as follows. The *x* axis was determined by the line crossing the center of mass of the two sister anaphase chromosome masses, the *z* axis was determined as the line perpendicular to the coverslip, and the *y* axis was defined as perpendicular to both *x* and *z* axes.

As no directionality of individual chromosome pairs along the *y* axis can be predetermined, all X chromosomes or one of homologous chromosomes in closest proximity to $y = 0$ were given a positive value along the *y* axis for cultured cells. Each homologous chromosome of a pair was assigned to be either a color/white based on its proximity to the *y* axis, when $y = 0$ (a color was assigned to most the proximal, and white the most distal) and mapped to generate the 3D overlay data.

Midpoint Analysis Using a 2D Coordinate System. A 2D coordinate system was established along the *y* axis, or a line crossing the furthest edges of the metaphase/anaphase cell based on TO-PRO3 staining. The minimum/maximum position along the *y* axis was based on TO-PRO3 staining was assigned ±50%, and the center of each mitotic chromosome mass was defined as 0%. The midpoint was calculated as the middle value between the relative positions of each homologous pair along the *y* axis. Relative positions were determined by using the position of the center of mass of individual homologous chromosomes, divided by the length of TO-PRO3 signal along the *y* axis to normalize for cell size.

Three-Dimensional Superimposed Homolog Contour Map Data. Contour maps were generated in ImageJ. The grayscale saturation represents the density of localization when the homologous chromosomes are overlaid in 3D. Isolines were generated with lines that connect contours that share the same gray value (i.e., one contour outlines an area with the same intensity). The 3D superimposed contour map was thresholded by highlighting the brightest 20% of the image for contrast. Individual homologous chromosomes of a pair were labeled and sorted according to proximity to the nuclear meridional plane. The scale bar reflects inverted pixel measurements. White/black regions indicate a level of maximum/minimum localizations, respectively. If the homologous chromosomes were in fixed positions, there would be a clustered area of high density/occurrence that reflects the colocalization frequency for each of the homologs. In addition, the mapped position of each homologous pair would also be identical for every cell.

Two-Dimensional Positional Analysis of Homologous Chromosomes. The 2D coordinate system was established along the *y* axis as described previously. The relative positions of individual homologous chromosomes were determined using the closest point to the center of the chromosome mass at metaphase, or the mitotic spindle at anaphase to reflect the centromeric position normalized to the TO-PRO3 staining for the particular mitotic cell. As stated previously, determining the centromeric position for individual homologs minimizes variations that could be attributed to an asymmetry in chromosome/rosette condensation. An example for the calculation of the normalization for centromere position at 5.92 μm for a mitotic chromosome mass that spans 8.96 μm along the *y* axis is (5.92 μm/8.96 μm) − 0.5*100 = +16%.

Statistical Analysis. A rose plot was generated in MATLAB to present the distribution/frequency of angles observed between multiple homologous chromosome pairs of various sizes (*SI Appendix*, Fig. S1*A*). The observed values were categorized to 10° intervals (18 total) within a range of 180°. The vector length reflects the number of mitotic cells that falls within each group. For example the expected values for a random distribution for 66 cells would be calculated as 66 cells/18 total 10° intervals = 3.67. A χ^2 analysis χ^2 (36) was then performed for the observed values against the expected values of 3.67 for each 10° interval and calculated for significance (*P* value).

A connected scatterplot graph for frequency distribution shows the relationship between a chromosome and its homologous partner in comparison with a nonhomologous partner (Fig. 1*F*). Our null hypothesis is that chromosomes have a random distance to their homologous partners, thus reflected in similar distribution to a heterologous chromosome. The values were calculated based on the relative frequency (number of mitotic cells measuring minimal distance at a particular interval/total mitotic cells) for a chromosome to its homologous partner or nonhomologous partner (X or Y chromosome). A Student's *t* test (36) was performed for the minimum distance values between chromosome 4 and its homolog compared with chromosome 4 to a heterologous chromosome (X or Y) and calculated for significance (*P* value). Note that 0–0.4 μm were grouped into a single distance interval as it is defined by the limit in confocal microscopy resolution.

A binomial probability distribution (35, 36) was employed for statistics wherein the null hypothesis is that sex and homologous chromosome pairs are randomly distributed in two hemispheres of a mitotic cell at metaphase/anaphase. For example, if distributions of chromosomes are random between two hemispheres of equal size in a cell at metaphase/anaphase, the probability of the first chromosome of a given pair's being positioned in one hemisphere will be 1. The probability for the second chromosome's being positioned in the other hemisphere is 0.5. Therefore, the probability, or P, that an individual of a pair of sex or homologous chromosomes is positioned to two separate hemispheres, or x, which consists of multiple cells, or n, can be calculated by the binomial formula: $b(x; n, P) = \{ n!/[x! (n - x)!] \} * Px * (1 - P)n - x$. If the *P* value is <0.05, this would allow for rejection of our null hypothesis. Center of mass calculations were used for hemisphere localization; however, chromosomes that were positioned with the majority of their staining along the boundary of the hemispheres, due to the limits of resolution, were scored to support the null hypothesis, which goes against our model, in the calculation of the one-tailed *P* value which gives rise to an underestimation of statistical significance.

We used linear regression analysis (36) to determine whether there is a relationship between chromosome size and position within the mitotic cell. The null hypothesis is that chromosome size does not correlate with position and can be visualized/represented with a trendline with a slope of 0. Subsequently, we then used a R^2 analysis to test whether the linear regression/trendline between chromosome size (the independent variable) can predict position (dependent variable) within the mitotic cell. The R^2 analysis reveals how close the actual data variation fits the modeled regression/trendline of the mean. For example, R^2 values of 0 provide no explanation of variation of the mean (i.e., chromosome size does not determine position in mitotic cell), while R^2 values of 1 provide that the modeled trendline explains all of the data variability around the mean (i.e., chromosome size does determine position in mitotic cell).

ACKNOWLEDGMENTS. We thank Dr. Alexey Khodjakov for providing the CENP-A/centrin1-GFP cells; Dr. Roger Reeves for his gift of the male Ts65Dn mice; Dr. Thomas Kornberg and Dr. Patrick O'Farrell for discussion and comments on the manuscript; Dr. Jeanette Hyer for critical reading of the manuscript; T.M. laboratory members for their comments and suggestions: Sara Venters, Michael Bressan, David Mai, Christina Sun, Jonathan Louie, Hao Wu, Brian Yang, Rieko Asai (for use of her MATLAB script), Lisandro Maya-Ramos, and Jan Schlueter; Dr. Ann Zovein and Zovein laboratory members Carlos Lizama, John Hawkins, Joan Zape, and Chris Schmitt for assistance with the animals and discussions regarding the project; Weiner laboratory members Jeffrey Alexander and Miriam Genuth for comments and discussions; and Scott Jereb, David Hua, Jane Liu, Robert Jereb, and Kathy Jereb for their support. We apologize to the colleagues whose work we could not cite due to space limitations. This work was supported in part by NIH Grants 5KL2TR001870-03 (to L.L.H.), R01HL122375 (to T.M.), R37HL078921 (to T.M.), and R01HL132832 (to T.M.).

1. Guirouilh-Barbat J, Lambert S, Bertrand P, Lopez BS (2014) Is homologous recombination really an error-free process? *Front Genet* 5:175.
2. Carvalho CMB, Lupski JR (2016) Mechanisms underlying structural variant formation in genomic disorders. *Nat Rev Genet* 17:224–238.
3. Colnaghi R, Carpenter G, Volker M, O'Driscoll M (2011) The consequences of structural genomic alterations in humans: Genomic disorders, genomic instability and cancer. *Semin Cell Dev Biol* 22:875–885.
4. Gupta PK, et al. (1997) High frequency in vivo loss of heterozygosity is primarily a consequence of mitotic recombination. *Cancer Res* 57:1188–1193.
5. Holt D, et al. (1999) Interindividual variation in mitotic recombination. *Am J Hum Genet* 65:1423–1427.
6. McKee BD (2004) Homologous pairing and chromosome dynamics in meiosis and mitosis. *Biochim Biophys Acta* 1677:165–180.
7. Tsai JH, McKee BD (2011) Homologous pairing and the role of pairing centers in meiosis. *J Cell Sci* 124:1955–1963.
8. Nagele R, Freeman T, McMorrow L, Lee HY (1995) Precise spatial positioning of chromosomes during prometaphase: Evidence for chromosomal order. *Science* 270: 1831–1835.
9. Nagele RG, et al. (1998) Chromosome spatial order in human cells: Evidence for early origin and faithful propagation. *Chromosoma* 107:330–338.
10. Allison DC, Nestor AL (1999) Evidence for a relatively random array of human chromosomes on the mitotic ring. *J Cell Biol* 145:1–14.
11. Bolzer A, et al. (2005) Three-dimensional maps of all chromosomes in human male fibroblast nuclei and prometaphase rosettes. *PLoS Biol* 3:e157.
12. Keneklis TP, Odartchenko N (1974) Autoradiographic visualisation of paternal chromosomes in mouse eggs. *Nature* 247:215–216.
13. Straight AF, Marshall WF, Sedat JW, Murray AW (1997) Mitosis in living budding yeast: Anaphase A but no metaphase plate. *Science* 277:574–578.
14. Aragón-Alcaide L, Strunnikov AV (2000) Functional dissection of in vivo interchromosome association in Saccharomyces cerevisiae. *Nat Cell Biol* 2:812–818.
15. Jain IH, Vijayan V, O'Shea EK (2012) Spatial ordering of chromosomes enhances the fidelity of chromosome partitioning in cyanobacteria. *Proc Natl Acad Sci USA* 109: 13638–13643.
16. Gerlich D, et al. (2003) Global chromosome positions are transmitted through mitosis in mammalian cells. *Cell* 112:751–764.
17. Essers J, et al. (2005) Dynamics of relative chromosome position during the cell cycle. *Mol Biol Cell* 16:769–775.
18. Strickfaden H, Zunhammer A, van Koningsbruggen S, Köhler D, Cremer T (2010) 4D chromatin dynamics in cycling cells: Theodor Boveri's hypotheses revisited. *Nucleus* 1: 284–297.
19. Magidson V, et al. (2011) The spatial arrangement of chromosomes during prometaphase facilitates spindle assembly. *Cell* 146:555–567.
20. Miyanari Y, Ziegler-Birling C, Torres-Padilla ME (2013) Live visualization of chromatin dynamics with fluorescent TALEs. *Nat Struct Mol Biol* 20:1321–1324.
21. Reichmann J, et al. (2018) Dual-spindle formation in zygotes keeps parental genomes apart in early mammalian embryos. *Science* 361:189–193.
22. Rieder CL, Khodjakov A (2003) Mitosis through the microscope: Advances in seeing inside live dividing cells. *Science* 300:91–96.
23. Rabbitts P, et al. (1995) Chromosome specific paints from a high resolution flow karyotype of the mouse. *Nat Genet* 9:369–375.
24. Cremer M, et al. (2008) Multicolor 3D fluorescence in situ hybridization for imaging interphase chromosomes. *Methods Mol Biol* 463:205–239.
25. Fung JC, Marshall WF, Dernburg A, Agard DA, Sedat JW (1998) Homologous chromosome pairing in Drosophila melanogaster proceeds through multiple independent initiations. *J Cell Biol* 141:5–20.
26. Muller WA, Gimbrone MA, Jr (1986) Plasmalemmal proteins of cultured vascular endothelial cells exhibit apical-basal polarity: Analysis by surface-selective iodination. *J Cell Biol* 103:2389–2402.
27. Walczak CE, Cai S, Khodjakov A (2010) Mechanisms of chromosome behaviour during mitosis. *Nat Rev Mol Cell Biol* 11:91–102.
28. Betterton MD, McIntosh JR (2013) Regulation of chromosome speeds in mitosis. *Cell Mol Bioeng* 6:418–430.
29. Mosgöller W, Leitch AR, Brown JK, Heslop-Harrison JS (1991) Chromosome arrangements in human fibroblasts at mitosis. *Hum Genet* 88:27–33.
30. Papoulis A (1984) Bernoulli trials. *Probability, Random Variables, and Stochastic Processes* (McGraw-Hill, New York), 2nd Ed, pp 57–63.
31. Dodge Y (2008) *The Concise Encyclopedia of Statistics* (Springer, New York), pp 38–39.
32. Ross MT, et al. (2005) The DNA sequence of the human X chromosome. *Nature* 434: 325–337.
33. Foe V (1993) Mitosis and morphogenesis in the Drosophila embryo: Point and counterpoint. *The Development of Drosophila Melanogaster* (Cold Spring Harbor Lab Press, Cold Spring Harbor, NY), Vol 1, pp 149–300.
34. Sonnenblick B (1950) The early embryology of Drosophila melanogaster. *Biology of Drosophila* (Wiley, New York), pp 62–167.
35. Huettner A (1924) Maturation and fertilization in Drosophila melanogaster. *J Morphol* 39:249–265.
36. Gondos B, Bhiraleus P (1970) Pronuclear relationship and association of maternal and paternal chromosomes in flushed rabbit ova. *Z Zellforsch Mikrosk Anat* 111:149–159.
37. Odartchenko N, Keneklis T (1973) Localization of paternal DNA in interphase nuclei of mouse eggs during early cleavage. *Nature* 241:528–529.
38. Brandriff BF, Gordon LA, Carrano AV (1990) Cytogenetics of human sperm: Structural aberrations and DNA replication. *Prog Clin Biol Res* 340B:425–434.
39. Mayer W, Smith A, Fundele R, Haaf T (2000) Spatial separation of parental genomes in preimplantation mouse embryos. *J Cell Biol* 148:629–634.
40. Nichols WW, et al. (1987) Cytogenetic evaluation of human endothelial cell cultures. *J Cell Physiol* 132:453–462.
41. Zhang L, et al. (2000) Loss of chromosome 13 in cultured human vascular endothelial cells. *Exp Cell Res* 260:357–364.
42. Weise A, et al. (2016) Chromosomes in a genome-wise order: Evidence for metaphase architecture. *Mol Cytogenet* 9:36.
43. Epstein CJ, Cox DR, Epstein LB (1985) Mouse trisomy 16: An animal model of human trisomy 21 (Down syndrome). *Ann N Y Acad Sci* 450:157–168.
44. Davisson MT, Schmidt C, Akeson EC (1990) Segmental trisomy of murine chromosome 16: A new model system for studying Down syndrome. *Prog Clin Biol Res* 360:263–280.
45. Reeves RH, et al. (1995) A mouse model for Down syndrome exhibits learning and behaviour deficits. *Nat Genet* 11:177–184.
46. Davisson MT, et al. (1993) Segmental trisomy as a mouse model for Down syndrome. *Prog Clin Biol Res* 384:117–133.
47. Akeson EC, et al. (2001) Ts65Dn–Localization of the translocation breakpoint and trisomic gene content in a mouse model for Down syndrome. *Cytogenet Cell Genet* 93:270–276.
48. Egel R, Lankenau D-H, eds (2007) *Recombination and Meiosis: Models, Means, and Evolution* (Springer, New York), pp 182–186.
49. Baudat F, Imai Y, de Massy B (2013) Meiotic recombination in mammals: Localization and regulation. *Nat Rev Genet* 14:794–806.
50. Roukos V, et al. (2013) Spatial dynamics of chromosome translocations in living cells. *Science* 341:660–664.
51. Joyce EF, Williams BR, Xie T, Wu CT (2012) Identification of genes that promote or antagonize somatic homolog pairing using a high-throughput FISH-based screen. *PLoS Genet* 8:e1002667.
52. Joyce EF, Erceg J, Wu C-T (2016) Pairing and anti-pairing: A balancing act in the diploid genome. *Curr Opin Genet Dev* 37:119–128.
53. Koeman JM, et al. (2008) Somatic pairing of chromosome 19 in renal oncocytoma is associated with deregulated EGLN2-mediated [corrected] oxygen-sensing response. *PLoS Genet* 4:e1000176.
54. Davisson M, et al. (2007) Impact of trisomy on fertility and meiosis in male mice. *Hum Reprod* 22:468–476.
55. Moore CS, et al. (2010) Increased male reproductive success in Ts65Dn "Down syndrome" mice. *Mamm Genome* 21:543–549.
56. Selvaraj S, Dixon JR, Bansal V, Ren B (2013) Whole-genome haplotype reconstruction using proximity-ligation and shotgun sequencing. *Nat Biotechnol* 31:1111–1118.
57. Rao SS, et al. (2014) A 3D map of the human genome at kilobase resolution reveals principles of chromatin looping. *Cell* 159:1665–1680.
58. Heride C, et al. (2010) Distance between homologous chromosomes results from chromosome positioning constraints. *J Cell Sci* 123:4063–4075.
59. Gandhi M, et al. (2012) Homologous chromosomes make contact at the sites of double-strand breaks in genes in somatic G0/G1-phase human cells. *Proc Natl Acad Sci USA* 109:9454–9459.
60. Bard F, Bourgeois CA, Costagliola D, Bouteille M (1985) Rotation of the cell nucleus in living cells: A quantitative analysis. *Biol Cell* 54:135–142.
61. Allen VW, Kropf DL (1992) Nuclear rotation and lineage specification in Pelvetia embryos. *Development* 115:873–883.
62. Tsou MF, Ku W, Hayashi A, Rose LS (2003) PAR-dependent and geometry-dependent mechanisms of spindle positioning. *J Cell Biol* 160:845–855.
63. Hua LL, Mikawa T (2018) Chromosome painting of mouse chromosomes. *Methods Mol Biol* 1752:133–143.
64. Duchon A, et al. (2011) Identification of the translocation breakpoints in the Ts65Dn and Ts1Cje mouse lines: Relevance for modeling Down syndrome. *Mamm Genome* 22: 674–684.
65. Agulnik AI, Bishop CE, Lerner JL, Agulnik SI, Solovyev VV (1997) Analysis of mutation rates in the SMCY/SMCX genes shows that mammalian evolution is male driven. *Mamm Genome* 8:134–138.
66. Kernohan KD, Bérubé NG (2014) Three dimensional dual labelled DNA fluorescent in situ hybridization analysis in fixed tissue sections. *MethodsX* 1:30–35.
67. Llères D, James J, Swift S, Norman DG, Lamond AI (2009) Quantitative analysis of chromatin compaction in living cells using FLIM-FRET. *J Cell Biol* 187:481–496.
68. Cheeseman IM, Desai A (2008) Molecular architecture of the kinetochore-microtubule interface. *Nat Rev Mol Cell Biol* 9:33–46.
69. Oliferenko S, Chew TG, Balasubramanian MK (2009) Positioning cytokinesis. *Genes Dev* 23:660–674.
70. Freshney RI (2011) Subculture and cell lines. *Culture of Animal Cells: A Manual of Basic Technique and Specialized Applications* (Wiley, New York), 6th Ed, pp 187–190.
71. Zhang J, et al. (2006) Neoplastic transformation of human diploid fibroblasts after long-term serum starvation. *Cancer Lett* 243:101–108.
72. Chen JG, Horwitz SB (2002) Differential mitotic responses to microtubule-stabilizing and -destabilizing drugs. *Cancer Res* 62:1935–1938.
73. Rohlf FJ, Rodman TC, Flehinger BJ (1980) The use of nonmetric multidimensional scaling for the analysis of chromosomal associations. *Comput Biomed Res* 13:19–35.
74. Aldrup-Macdonald ME, Sullivan BA (2014) The past, present, and future of human centromere genomics. *Genes (Basel)* 5:33–50.
75. Fukagawa T, Earnshaw WC (2014) The centromere: Chromatin foundation for the kinetochore machinery. *Dev Cell* 30:496–508.